Chinese Journal of Aeronautics, (2022), 35(6): 250–261

Chinese Society of Aeronautics and Astronautics
& Beihang University

Chinese Journal of Aeronautics

cja@buaa.edu.cn
www.sciencedirect.com

Sub-optimal fixed-finite-horizon spacecraft configuration control on SE(3)

Yulin WANG [a], **Wei SHANG** [b], **Haichao HONG** [c,*]

[a] *Institute of Remote-sensing Satellite, China Academy of Space Technology, Beijing 100094, China*
[b] *School of Mechanical Engineering, Hubei University of Technology, Wuhan 430068, China*
[c] *Institute of Flight System Dynamics, Technical University of Munich, Garching 85748, Germany*

Received 8 January 2021; revised 29 March 2021; accepted 29 May 2021
Available online 22 October 2021

KEYWORDS

Configuration control;
Lie groups;
Model Predictive Static Programming;
Optimal control;
Spacecraft control

Abstract For achieving the desired configuration of spacecraft at the desired fixed time, a sub-optimal fixed-finite-horizon configuration control method on the Lie group SE(3) is developed based on the Model Predictive Static Programming (MPSP). The MPSP technique has been widely used to solve finite-horizon optimal control problems and is known for its high computational efficiency thanks to the closed-form solution, but it cannot be directly applied to systems on SE(3). The methodological innovation in this paper enables that the MPSP technique is extended to the geometric control on SE(3), using the variational principle, the left-invariant properties of Lie groups, and the topology structure of Lie algebra space. Moreover, the energy consumption, which is crucial for spacecraft operations, is considered as the objective function to be optimized in the optimal control formulation. The effectiveness of the designed sub-optimal control method is demonstrated through an online simulation under disturbances and state measurement errors.

1. Introduction

For space missions, precision control of spacecraft is essential and has attracted considerable attention.[1–3] The integrated attitude and orbit tracking of a six-degree-of-freedom (6-DOF) spacecraft is one of the key technologies, e.g., for autonomous rendezvous and docking,[4,5] hovering over an asteroid,[6–9] and spacecraft formation flying.[10–13] Compared with the traditional modeling scheme whose attitude and position are modeled separately,[14–16] the integrated modeling scheme includes the mutual couplings between attitude and position, leading to a higher accuracy.

A 3-dimensional Special Euclidean group (SE(3)) can describe uniquely and globally the integrated attitude and position of a 6-DOF spacecraft in a 3-dimensional Euclidean space. In this modeling scheme, the mutual couplings between attitude and position are considered. In addition, the singularities and ambiguities of attitude representations are avoided. Thanks to these advantages, controlling 6-DOF rigid-body spacecraft modeled on SE(3), which are often referred as "geometric" control, has been widely researched by pioneers, e.g., by Bullo and Murray [17,18], Lee et al.[4,6–8,10,11]. In the existing studies, the PD control theory[17,18], the sliding mode control theory[10,8], and the fixed-time convergence control theory[4,6,19] are applied. Moreover, the control force saturation is considered in Ref. 7. In Ref. 11, a decentralized collision-avoidance control scheme is designed for spacecraft formation flying

* Corresponding author.
E-mail address: haichao.hong@tum.de (H. HONG).

https://doi.org/10.1016/j.cja.2021.07.023

based on artificial potentials. These geometric control schemes do not consider minimizing the energy consumption. Actually, the stored fuel of an in-orbit spacecraft is usually limited. Therefore, the energy consumption during the maneuver should be optimized to extend the operating life of spacecraft.

Under the general concept of Model Predictive Control (MPC), the energy consumption can be considered.[20,21] MPC techniques have been applied to the mechanical systems modeled on the Lie group SO(3)[22,23] and SE(3)[24]. However, these optimal control problem on Lie groups in Refs. 22–24 are all constructed and solved based on the linearized equations around their equilibrium points, and the algebraic Riccati equations need to be solved. In the optimal control schemes designed in Refs. 25–28, the nonlinear dynamics on SE(3) are considered. However, in Refs. 25,26, the two point boundary value problems need to be solved, which yields a high computational complexity. In Refs. 27,28, only the kinematics characteristics are studied in the optimal controller on SE(3).

Combining the philosophies of Approximate Dynamic Programming (ADP)[29] and MPC, Padhi proposed a finite-horizon optimal control method with hard terminal constraints called the Model Predictive Static Programming (MPSP).[30] The MPSP generates explicit closed-form solutions without relying on numerical optimization solver. Studies based on the MPSP and its varieties have been carried out in fields of aeronautics[31–33] and astronautics[34–36]. However, the commonly used MPSP technique in Ref. 30 and its varieties can only be used to solve an explicit discrete-time nonlinear dynamical system. Since SE(3) is a Lie group and a 6-dimensional manifold, its discrete-time nonlinear dynamical equation obtained from the Lie Group Variational Integrator (LGVI) is implicit.[25,37] Hence, the implementation of the commonly used MPSP is not yet feasible on SE(3).

This paper develops the intermediate steps that enable the application of the MPSP on SE(3), and thus achieves a sub-optimal fixed-finite-horizon control on SE(3), optimizing the overall energy consumption. Firstly, the dynamical equations of the spacecraft modeled on SE(3) are normalized, and thus the state variables on SE(3) have a similar numerical range. Then, based on the variational principle, the left-invariant properties of Lie groups, and the topology structure of Lie algebra space, the MPSP technique is extended to the geometric sub-optimal control on SE(3). The terminal output error between the predicted terminal states and desired states is defined as the exponential coordinate of SE(3). Lastly, taking advantages of the high efficiency, the proposed sub-optimal control scheme on SE(3) is applied online in a shrinking horizon, where the system disturbance and the state measurement errors are considered. Offline and online simulation studies are carried out to demonstrate the effectiveness of the proposed control schemes.

Compared with the MPC designed on SE(3) in Ref. 24, the proposed method makes use of the full nonlinear dynamics. Compared with the works in Refs. 27,28, both the kinematics and dynamics of the spacecraft on SE(3) are taken into consideration. Moreover, the proposed sub-optimal control method on SE(3) based on the MPSP has a higher computational efficiency, compared with the two point boundary value problems in Refs. 25,26 and the algebraic Riccati equations solved in Ref. 24. Compared with the previous work in Ref. 36, the positional dynamics of spacecraft are considered and the MPSP is further applied on SE(3) based on the normalized dynamical equations. Moreover, the terminal output error is designed based on the exponential coordinates of Lie group.

The rest of this paper is organized as follows. In Section 2, the dynamical equations of a 6-DOF spacecraft modeled on SE(3) are given. In Section 3, the proposed sub-optimal control scheme on SE(3) is deduced and designed. In Section 4, the results of numerical simulation are shown. In Section 5, the conclusions of this paper are summarized.

2. SE(3) modeling scheme for spacecraft configuration

In this section, the details of the modeling scheme are presented. The kinematics and dynamics of a fully actuated rigid-body spacecraft are described globally on SE(3). The body-fixed frame and the inertial reference frame are denoted as B-Frame and I-Frame, respectively.

The Lie group $\mathrm{SE}(3) = \mathrm{SO}(3) \times \mathbf{R}^3$ is the set including the attitude and position. The configuration of a rigid-body spacecraft with respect to I-Frame is denoted as $\boldsymbol{g} \in \mathrm{SE}(3)$, which can be represented by the following 4×4 matrix as

$$\boldsymbol{g} = \begin{bmatrix} \boldsymbol{R} & \boldsymbol{p} \\ 0_{1\times 3} & 1 \end{bmatrix} \in \mathrm{SE}(3) \tag{1}$$

where $\boldsymbol{p} \in \mathbf{R}^3$ represents the position of spacecraft. $\boldsymbol{R} \in \mathrm{SO}(3)$ is the attitude of spacecraft and represents the rotation matrix from B-Frame to I-Frame. SO(3) (the three-dimensional Special Orthogonal group) is also a Lie group with 9 elements and 6 constraints. SO(3) is expressed as

$$\mathrm{SO}(3) = \left\{ \boldsymbol{R} \in \mathbf{R}^{3\times 3} | \boldsymbol{R}^{\mathrm{T}}\boldsymbol{R} = \boldsymbol{I}, \det[\boldsymbol{R}] = 1 \right\} \tag{2}$$

The velocity and angular velocity of a 6-DOF spacecraft in B-Frame are represented by $\boldsymbol{V} \in \mathbf{R}^3$ and $\boldsymbol{\Omega} \in \mathbf{R}^3$, respectively. Then, the generalized velocity $\boldsymbol{\xi} \in \mathbf{R}^6$ in B-Frame is defined as

$$\boldsymbol{\xi} = \begin{bmatrix} \boldsymbol{\Omega} \\ \boldsymbol{V} \end{bmatrix} \in \mathbf{R}^6 \tag{3}$$

The kinematics of the rigid-body spacecraft expressed on SE(3) are

$$\dot{\boldsymbol{g}} = \boldsymbol{g}\boldsymbol{\xi}^{-} \tag{4}$$

where $[\cdot]^{-} : \mathbf{R}^6 \to \mathrm{se}(3)$ is a bijection map. $\mathrm{se}(3) = \mathrm{so}(3) \times \mathbf{R}^3$ and so(3) are the corresponding Lie algebras of the Lie groups SE(3) and SO(3), respectively. $\boldsymbol{\xi}^{-} \in \mathrm{se}(3)$ is expressed as

$$\boldsymbol{\xi}^{-} = \begin{bmatrix} \boldsymbol{\Omega} \\ \boldsymbol{V} \end{bmatrix}^{-} = \begin{bmatrix} \boldsymbol{\Omega}^{\wedge} & \boldsymbol{V} \\ 0_{1\times 3} & 0 \end{bmatrix} \tag{5}$$

where $[\cdot]^{\wedge} : \mathbf{R}^3 \to \mathrm{so}(3)$ denotes the skew-symmetric matrix operation and $\boldsymbol{\Omega}^{\wedge} \in \mathrm{so}(3)$ is expressed as

$$\boldsymbol{\Omega}^{\wedge} = \begin{bmatrix} \boldsymbol{\Omega}_1 \\ \boldsymbol{\Omega}_2 \\ \boldsymbol{\Omega}_3 \end{bmatrix}^{\wedge} = \begin{bmatrix} 0 & -\boldsymbol{\Omega}_3 & \boldsymbol{\Omega}_2 \\ \boldsymbol{\Omega}_3 & 0 & -\boldsymbol{\Omega}_1 \\ -\boldsymbol{\Omega}_2 & \boldsymbol{\Omega}_1 & 0 \end{bmatrix} \in \mathrm{so}(3) \tag{6}$$

The inverse maps of $[\cdot]^{\wedge} : \mathbf{R}^3 \to \mathrm{so}(3)$ and $[\cdot]^{-} : \mathbf{R}^6 \to \mathrm{se}(3)$ are $[\cdot]^{\vee} : \mathrm{so}(3) \to \mathbf{R}^3$ and $[\cdot]^{|} : \mathrm{se}(3) \to \mathbf{R}^6$, respectively.

The dynamics of 6-DOF spacecraft expressed on SE(3) are

$$\boldsymbol{I}\dot{\boldsymbol{\xi}} = \mathrm{ad}^{*}_{\boldsymbol{\xi}}\boldsymbol{I}\boldsymbol{\xi} + \boldsymbol{f} + \boldsymbol{d} \tag{7}$$

where $\boldsymbol{I} \in \mathbf{R}^{6\times 6}$ is the inertial parameters and determined by the inertial matrix $\boldsymbol{J} \in \mathbf{R}^{3\times 3}$ and mass $m \in \mathbf{R}_{+}$ of rigid-body space-

craft. The kinematic energy of spacecraft is calculated by $\frac{1}{2}\boldsymbol{\xi}^{\mathrm{T}}\boldsymbol{I}\boldsymbol{\xi}=\frac{1}{2}\boldsymbol{\Omega}^{\mathrm{T}}\boldsymbol{J}\boldsymbol{\Omega}+\frac{1}{2}m\boldsymbol{V}^{\mathrm{T}}\boldsymbol{V}$. $\boldsymbol{I}$ is expressed as

$$\boldsymbol{I}=\begin{bmatrix}\boldsymbol{J} & 0_{3\times3}\\ 0_{3\times3} & m\boldsymbol{I}_{3\times3}\end{bmatrix} \tag{8}$$

Moreover, $\mathrm{ad}_{\xi}^{*}=(\mathrm{ad}_{\xi})^{\mathrm{T}}$ is the co-adjoint operation, which is the dual operation of ad_{ξ}, and $\mathrm{ad}_{\xi}:\mathbf{R}^6\rightarrow\mathbf{R}^6$ is the adjoint operator. The matrix form of ad_{ξ} is

$$\mathrm{ad}_{\xi}=\begin{bmatrix}\boldsymbol{\Omega}^{\wedge} & 0_{3\times3}\\ \boldsymbol{V}^{\wedge} & \boldsymbol{\Omega}^{\wedge}\end{bmatrix}\in\mathbf{R}^{6\times6} \tag{9}$$

Where $\boldsymbol{f}\in\mathbf{R}^6$ is the generalized input action of 6-DOF spacecraft in B-Frame. $\boldsymbol{d}\in\mathbf{R}^6$ is the generalized external disturbance acting on spacecraft. $\boldsymbol{d}$ is caused by model reductions and parameter uncertainties. The generalized forces $\boldsymbol{f}$ and $\boldsymbol{d}$ are expressed as

$$\boldsymbol{u}=\begin{bmatrix}\boldsymbol{\tau}\\ \boldsymbol{F}\end{bmatrix},\quad \boldsymbol{d}=\begin{bmatrix}\boldsymbol{d}_{\Omega}\\ \boldsymbol{d}_{V}\end{bmatrix} \tag{10}$$

where $\boldsymbol{\tau}\in\mathbf{R}^3$ and $\boldsymbol{F}\in\mathbf{R}^3$ are input torque and force, respectively. $\boldsymbol{d}_{\Omega}\in\mathbf{R}^3$ and $\boldsymbol{d}_{V}\in\mathbf{R}^3$ are disturbance torque and force, respectively.

Considering the definitions and deductions above, the kinematics and dynamics of 6-DOF spacecraft in Eqs. (4) and (7) are reformulated as Eqs. (11)–(14).

$$\dot{\boldsymbol{R}}=\boldsymbol{R}\boldsymbol{\Omega}^{\wedge} \tag{11}$$

$$\dot{\boldsymbol{p}}=\boldsymbol{R}\boldsymbol{V} \tag{12}$$

$$\boldsymbol{J}\dot{\boldsymbol{\Omega}}=-\boldsymbol{\Omega}\times\boldsymbol{J}\boldsymbol{\Omega}+\boldsymbol{\tau}+\boldsymbol{d}_{\Omega} \tag{13}$$

$$m\dot{\boldsymbol{V}}=-\boldsymbol{\Omega}\times m\boldsymbol{V}+\boldsymbol{F}+\boldsymbol{d}_{V} \tag{14}$$

The relative rotation angle between the current and desired attitudes of spacecraft is usually bounded by π rad. However, the relative distance between the current and desired positions is unlimited. In order to ensure a similar numerical range for all state variables, the state variables of the translational subsystem can be normalized as follows

$$\boldsymbol{p}'=\frac{\boldsymbol{p}}{p_{\mathrm{m}}},\quad \boldsymbol{V}'=\frac{\boldsymbol{V}}{V_{\mathrm{m}}} \tag{15}$$

where $\boldsymbol{p}'\in\mathbf{R}^3$ and $\boldsymbol{V}'\in\mathbf{R}^3$ are the normalized values for $\boldsymbol{p}$ and $\boldsymbol{V}$, respectively. $p_{\mathrm{m}},V_{\mathrm{m}}\in\mathbf{R}$ are the normalizing quantities. Then, the normalized versions of Eqs. (11)–(14) are obtained as

$$\begin{cases}\dot{\boldsymbol{R}}=\boldsymbol{R}\boldsymbol{\Omega}^{\wedge}\\ p_{\mathrm{m}}\dot{\boldsymbol{p}}'=V_{\mathrm{m}}\boldsymbol{R}\boldsymbol{V}'\\ \boldsymbol{J}\dot{\boldsymbol{\Omega}}=-\boldsymbol{\Omega}\times\boldsymbol{J}\boldsymbol{\Omega}+\boldsymbol{\tau}+\boldsymbol{d}_{\Omega}\\ mV_{\mathrm{m}}\dot{\boldsymbol{V}}'=-\boldsymbol{\Omega}\times mV_{\mathrm{m}}\boldsymbol{V}'+\boldsymbol{F}+\boldsymbol{d}_{V}\end{cases} \tag{16}$$

3. Sub-optimal fixed-finite-horizon configuration control based on the MPSP

In this section, a sub-optimal fixed-finite-horizon configuration control on SE(3) is deduced and designed based on the MPSP technique. The general derivations and design processes of the original MPSP on an Euclidean space can be found in Appendix A. However, SE(3) is a six-dimensional nonlinear manifold with 16elements and 10constraints. The general designing procedure of the MPSP in Appendix A cannot be applied on SE(3). This problem will be detailed and resolved by the theory of differential geometry in this section.

3.1. Discrete-time dynamics on SE(3)

Before the sub-optimal control scheme is constructed, the system described by Eq. (16) should be discretized with time. Since SE(3) is a Lie group, commonly used numerical integration methods, such as the Euler integration, cannot preserve its underlying group structure. Therefore, the Lie Group Variational Integrator (LGVI) is applied here to provide the discrete-time nonlinear dynamical system on SE(3). From the continuous dynamical system in Eq. (16), the LGVI-based discrete-time nonlinear dynamics of 6-DOF spacecraft system modeled on SE(3) are expressed as Eqs. (17)–(21) [25,37]

$$\boldsymbol{R}_{k+1}=\boldsymbol{R}_k\boldsymbol{f}_k \tag{17}$$

$$\boldsymbol{f}_k\boldsymbol{J}_{\mathrm{d}}-\boldsymbol{J}_{\mathrm{d}}\boldsymbol{f}_k^{\mathrm{T}}=h(\boldsymbol{J}\boldsymbol{\Omega}_k)^{\wedge} \tag{18}$$

$$\boldsymbol{p}'_{k+1}=\boldsymbol{p}'_k+\frac{hV_{\mathrm{m}}}{p_{\mathrm{m}}}\boldsymbol{R}_k\boldsymbol{V}'_k \tag{19}$$

$$\boldsymbol{J}\boldsymbol{\Omega}_{k+1}=\boldsymbol{f}_k^{\mathrm{T}}\boldsymbol{J}\boldsymbol{\Omega}_k+h\boldsymbol{\tau}_k \tag{20}$$

$$m\boldsymbol{V}'_{k+1}=\boldsymbol{f}_k^{\mathrm{T}}m\boldsymbol{V}'_k+\frac{h}{V_{\mathrm{m}}}\boldsymbol{F}_k \tag{21}$$

where $\boldsymbol{J}_{\mathrm{d}}\in\mathbf{R}^{3\times3}$ is a nonstandard moment of inertia matrix defined as $\boldsymbol{J}_{\mathrm{d}}=1/2\mathrm{tr}(\boldsymbol{J})\boldsymbol{I}-\boldsymbol{J}$. $\boldsymbol{R}_k\in\mathrm{SO}(3)$ and $\boldsymbol{\Omega}_k\in\mathbf{R}^3$ are the attitude and angular velocity of spacecraft at step $k,k=1,2,\ldots,N-1$, respectively. $\boldsymbol{p}'_k\in\mathbf{R}^3$ and $\boldsymbol{V}'_k\in\mathbf{R}^3$ are the normalized position and velocity of spacecraft at step k, respectively. $\boldsymbol{f}_k\in\mathrm{SO}(3)$ is the group change in $\boldsymbol{R}_k$, which is related to the angular velocity $\boldsymbol{\Omega}_k\in\mathbf{R}^3$ as shown in Eq. (18). $\boldsymbol{\tau}_k\in\mathbf{R}^3$ and $\boldsymbol{F}_k\in\mathbf{R}^3$ are the external input torque and force, respectively. h is the length of integration step. In the discrete-time nonlinear dynamical system described by Eqs. (17)–(21), the state $\boldsymbol{X}_k$, output $\boldsymbol{Y}_k$ and input $\boldsymbol{U}_k$ are set as

$$\begin{cases}\boldsymbol{X}_k=\begin{bmatrix}\boldsymbol{R}_k, & \boldsymbol{p}'_k, & \boldsymbol{\Omega}_k, & \boldsymbol{V}'_k\end{bmatrix}\\ \boldsymbol{Y}_k=\begin{bmatrix}\boldsymbol{R}_k, & \boldsymbol{p}'_k, & \boldsymbol{\Omega}_k, & \boldsymbol{V}'_k\end{bmatrix}\\ \boldsymbol{U}_k=\begin{bmatrix}\boldsymbol{\tau}_k, & \boldsymbol{F}'_k\end{bmatrix}\end{cases} \tag{22}$$

where $\boldsymbol{F}'_k=\frac{\boldsymbol{F}_k}{V_{\mathrm{m}}}$ is the normalized force. From Refs. 38,25, the propagations of Eqs. (17)–(21) can be obtained as shown in Fig. 1.

Eq. (18) is an implicit equation with respect to $\boldsymbol{f}_k$, and $\boldsymbol{f}_k$ can be only solved via numerical solutions such as Newton iteration. This differentiates from the general discrete-time nonlinear dynamical equation described by Eq. (A1) in Appendix A. Moreover, $\boldsymbol{R}_k,\boldsymbol{f}_k$ are the nonlinear matrices belonging to SO(3) and the Jacobian matrices of Eqs. (17)–(21) are hard to calculated. Therefore, many optimal control techniques, such as the MPSP, are hard to applied on SE(3) directly based on Eqs. (17)–(21).

3.2. MPSP on SE(3)

Because of the implicit LGVI-based discrete-time nonlinear dynamical expression of SE(3) in Eqs. (17)–(21) and the Lie

group $\boldsymbol{R}_k$ included in the state $\boldsymbol{X}_k$, the general MPSP technique in Appendix A cannot be applied on SE(3). This subsection provides new insight into applying the MPSP technique on the Lie group SE(3) based on the variational principle, the left-invariant properties of Lie groups, and the topology structure of so(3).[39,40]

The terminal output and the desired output of the discrete-time system in Eqs. (17)–(21) are denoted as $\boldsymbol{Y}_N$ and $\boldsymbol{Y}_\mathrm{d}$, respectively. The primary objective of this paper is designing a suitable control series $\boldsymbol{U}_k, k = 1, 2, \ldots, N-1$ for the discrete-time dynamical system described by Eqs. (17)–(21), in order to let $\boldsymbol{Y}_N$ reach to $\boldsymbol{Y}_\mathrm{d}$ with the minimal energy consumption. The optimal control problem is summarized as

$$\begin{aligned} \min_{\boldsymbol{U}_k} \quad & J = \tfrac{1}{2}\sum_{k=1}^{N-1} \boldsymbol{U}_k^{\mathrm{T}} \boldsymbol{Q}_k \boldsymbol{U}_k \\ \text{s.t.} \quad & \text{Eqs.}(17)-(21) \\ & \boldsymbol{Y}_N = \boldsymbol{Y}_\mathrm{d} \end{aligned} \tag{23}$$

where J is the objective function that optimizes the energy consumption. $\boldsymbol{Q}_k > \boldsymbol{0} \in \mathbf{R}^{m\times m}$ is the weighting matrix. Here, $\boldsymbol{U}_k$ is assumed to be independent of the states and control inputs in the previous steps.

The error between $\boldsymbol{Y}_N$ and $\boldsymbol{Y}_\mathrm{d}$ is denoted as $\mathrm{d}\boldsymbol{Y}_N$. First, resembling the general MPSP technique in Appendix A, $\mathrm{d}\boldsymbol{Y}_N$ should be expressed by the infinitesimal variations of $\boldsymbol{U}_k, \mathrm{d}\boldsymbol{U}_k$. With the definition of $\boldsymbol{Y}_k$ in Eq. (22), $\mathrm{d}\boldsymbol{Y}_N$ is expressed as

$$\mathrm{d}\boldsymbol{Y}_N = \begin{bmatrix} \mathrm{d}\boldsymbol{R}_k, & \mathrm{d}\boldsymbol{p}'_k, & \mathrm{d}\boldsymbol{\Omega}_k, & \mathrm{d}\boldsymbol{V}'_k \end{bmatrix} \tag{24}$$

The implicit expressions of the discrete-time nonlinear dynamics in Eqs. (17)–(21) are mainly caused by $\boldsymbol{R}_k \in \mathrm{SO}(3)$ because SO(3) is a nonlinear manifold with 9 elements and 6 constraints as shown in Eq. (2). In Eq. (24), $\mathrm{d}\boldsymbol{R}_k \in T_{\boldsymbol{R}_k}\mathrm{SO}(3)$ is a matrix, whose corresponding continuous variable $\mathrm{d}\boldsymbol{R}$ can be expressed as

$$\mathrm{d}\boldsymbol{R} = \boldsymbol{R}\boldsymbol{\eta}^\wedge \tag{25}$$

where $\boldsymbol{\eta} \in \mathbf{R}^3$ and $\boldsymbol{\eta}^\wedge \in \mathrm{so}(3)$. Using the left-invariant properties of Lie groups, and the topology structure of so(3), where so(3) is differential homeomorphism to $\mathbf{R}^3, \mathrm{d}\boldsymbol{R}$ can then be expressed by $\boldsymbol{\eta}$ properly. Moreover, the continuous dynamics of $\boldsymbol{\eta}$ is obtained from Refs. 39,40 as

$$\dot{\boldsymbol{\eta}} = \mathrm{d}\boldsymbol{\Omega} - \boldsymbol{\Omega}^\wedge \boldsymbol{\eta} \tag{26}$$

The infinitesimal variations of $\dot{\boldsymbol{p}}', \dot{\boldsymbol{\Omega}}$ and $\dot{\boldsymbol{V}}'$ are deduced from Eq.(16) as

$$\mathrm{d}\dot{\boldsymbol{p}}' = \frac{V_\mathrm{m}}{p_\mathrm{m}}\boldsymbol{R}\boldsymbol{\eta}^\wedge \boldsymbol{V}' + \frac{V_\mathrm{m}}{p_\mathrm{m}}\boldsymbol{R}\mathrm{d}\dot{\boldsymbol{V}}' \tag{27}$$

$$\mathrm{d}\dot{\boldsymbol{\Omega}} = \boldsymbol{J}^{-1}\left((\boldsymbol{J}\boldsymbol{\Omega})^\wedge - \boldsymbol{\Omega}^\wedge \boldsymbol{J}\right)\mathrm{d}\boldsymbol{\Omega} + \boldsymbol{J}^{-1}\mathrm{d}\boldsymbol{\tau} \tag{28}$$

$$\mathrm{d}\dot{\boldsymbol{V}}' = \boldsymbol{V}'^\wedge \mathrm{d}\boldsymbol{\Omega} - \boldsymbol{\Omega}^\wedge \mathrm{d}\boldsymbol{V}' + \frac{1}{m}\mathrm{d}\boldsymbol{F}' \tag{29}$$

Since $\mathrm{d}\boldsymbol{R}$ can be represented by $\boldsymbol{\eta}$ identically, the infinitesimal variation of the state $\boldsymbol{X}$ in Eq. (22) is given identically as

$$\mathrm{d}\boldsymbol{X} \triangleq \begin{bmatrix} \boldsymbol{\eta} \\ \mathrm{d}\boldsymbol{p}' \\ \mathrm{d}\boldsymbol{\Omega} \\ \mathrm{d}\boldsymbol{V}' \end{bmatrix} \in \mathbf{R}^{12} \tag{30}$$

Moreover, the infinitesimal variations of the output $\boldsymbol{Y}$ and input $\boldsymbol{U}$ in Eq. (22) are given in Eq. (31) and Eq. (32), respectively.

$$\mathrm{d}\boldsymbol{Y} = \begin{bmatrix} \boldsymbol{\eta} \\ \mathrm{d}\boldsymbol{p}' \\ \mathrm{d}\boldsymbol{\Omega} \\ \mathrm{d}\boldsymbol{V}' \end{bmatrix} \in \mathbf{R}^{12} \tag{31}$$

$$\mathrm{d}\boldsymbol{U} = \begin{bmatrix} \mathrm{d}\boldsymbol{\tau} \\ \mathrm{d}\boldsymbol{F}' \end{bmatrix} \in \mathbf{R}^{6} \tag{32}$$

Then, Eqs. (26)–(29) form a special continuous dynamical system, whose states, inputs, and outputs are $\mathrm{d}\boldsymbol{X}, \mathrm{d}\boldsymbol{U}$, and $\mathrm{d}\boldsymbol{Y}$, respectively. From Eqs. (26)–(29), the continuous dynamical expression of $\mathrm{d}\boldsymbol{X}$ is

$$\begin{aligned} \mathrm{d}\dot{\boldsymbol{X}} = & \begin{bmatrix} -\boldsymbol{\Omega}^\wedge & 0 & \boldsymbol{I} & 0 \\ -\frac{V_\mathrm{m}}{p_\mathrm{m}}\boldsymbol{R}\boldsymbol{V}'^\wedge & 0 & 0 & \frac{V_\mathrm{m}}{p_\mathrm{m}}\boldsymbol{R} \\ 0 & 0 & \boldsymbol{J}^{-1}\left((\boldsymbol{J}\boldsymbol{\Omega})^\wedge - \boldsymbol{\Omega}^\wedge \boldsymbol{J}\right) & 0 \\ 0 & 0 & \boldsymbol{V}'^\wedge & -\boldsymbol{\Omega}^\wedge \end{bmatrix} \mathrm{d}\boldsymbol{X} \\ & + \begin{bmatrix} 0 & 0 \\ 0 & 0 \\ \boldsymbol{J}^{-1} & 0 \\ 0 & \frac{1}{m}\boldsymbol{I} \end{bmatrix} \mathrm{d}\boldsymbol{U} \end{aligned} \tag{33}$$

In order to apply the MPSP technique, the model dynamics should be of a discrete form, and for $\mathrm{d}\boldsymbol{X} \in \mathbf{R}^{12}$, the Forward Euler integration scheme can be used here. Then, the discrete-time form of Eq. (33) is expressed as

$$\begin{aligned} \mathrm{d}\boldsymbol{X}_{k+1} &= \mathrm{d}\boldsymbol{X}_k + h\mathrm{d}\dot{\boldsymbol{X}}_k \\ &= \boldsymbol{A}'_k \mathrm{d}\boldsymbol{X}_k + \boldsymbol{B}'_k \mathrm{d}\boldsymbol{U}_k \end{aligned} \tag{34}$$

where $\boldsymbol{A}'_k \in \mathbf{R}^{12\times 12}, \boldsymbol{B}'_k \in \mathbf{R}^{12\times 6}$ are

$$\begin{cases} \boldsymbol{A}'_k = \begin{bmatrix} \boldsymbol{I} - h\boldsymbol{\Omega}_k^\wedge & 0 & h\boldsymbol{I} & 0 \\ -\frac{hV_\mathrm{m}}{p_\mathrm{m}}\boldsymbol{R}_k\boldsymbol{V}_k'^\wedge & \boldsymbol{I} & 0 & \frac{hV_\mathrm{m}}{p_\mathrm{m}}\boldsymbol{R}_k \\ 0 & 0 & \boldsymbol{I} - h\boldsymbol{J}^{-1}\left((\boldsymbol{J}\boldsymbol{\Omega}_k)^\wedge - \boldsymbol{\Omega}_k^\wedge \boldsymbol{J}\right) & 0 \\ 0 & 0 & h\boldsymbol{V}_k'^\wedge & \boldsymbol{I} - h\boldsymbol{\Omega}_k^\wedge \end{bmatrix} \\ \boldsymbol{B}'_k = \begin{bmatrix} 0 & 0 \\ 0 & 0 \\ h\boldsymbol{J}^{-1} & 0 \\ 0 & \frac{h}{m}\boldsymbol{I} \end{bmatrix} \end{cases} \tag{35}$$

Considering Eq. (34), the infinitesimal variation of $\boldsymbol{X}_{k+1}$ can be represented by the infinitesimal variations of $\boldsymbol{X}_k$ and $\boldsymbol{U}_k$, which corresponds to Eq. (A4) for the general MPSP technique in Appendix A.

With the definitions of $\boldsymbol{X}_k$ and $\boldsymbol{Y}_k$ in Eq. (22), $\mathrm{d}\boldsymbol{Y}_N$ in Eq. (24) can be expressed as

$$\mathrm{d}\boldsymbol{Y}_N = \mathrm{d}\boldsymbol{X}_N \tag{36}$$

Based on Eq. (34), $\mathrm{d}\boldsymbol{X}_N$ can be expressed by $\mathrm{d}\boldsymbol{X}_{N-1}$ and $\mathrm{d}\boldsymbol{U}_{N-1}$. Then, Eq. (36) is deduced as

$$\mathrm{d}\boldsymbol{Y}_N = \boldsymbol{A}'_{N-1}\mathrm{d}\boldsymbol{X}_{N-1} + \boldsymbol{B}'_{N-1}\mathrm{d}\boldsymbol{U}_{N-1} \tag{37}$$

Similar to the expression of $\mathrm{d}\boldsymbol{X}_N, \mathrm{d}\boldsymbol{X}_{N-1}$ can be also expressed by $\mathrm{d}\boldsymbol{X}_{N-2}$ and $\mathrm{d}\boldsymbol{U}_{N-2}$. Repeating this procedure until $k = 1, \mathrm{d}\boldsymbol{Y}_N$ can be deduced and expanded as

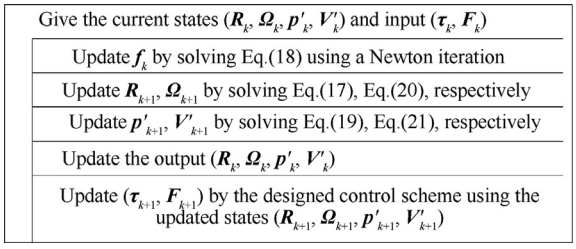

Fig. 1 Nassi Shneiderman diagram for the propagations of Eqs. (17)–(21).

$$\mathrm{d}\boldsymbol{Y}_N = \boldsymbol{A}\mathrm{d}\boldsymbol{X}_1 + \boldsymbol{B}_1\mathrm{d}\boldsymbol{U}_1 + \boldsymbol{B}_2\mathrm{d}\boldsymbol{U}_2 + \cdots + \boldsymbol{B}_{N-1}\mathrm{d}\boldsymbol{U}_{N-1} \tag{38}$$

where $\boldsymbol{A}, \boldsymbol{B}_k, k = 1, 2, \ldots, N-2$ and $\boldsymbol{B}_{N-1}$ are expressed as

$$\begin{cases} \boldsymbol{A} \triangleq \boldsymbol{A}'_{N-1}\boldsymbol{A}'_{N-2}\cdots\boldsymbol{A}'_1 \\ \boldsymbol{B}_k \triangleq \boldsymbol{A}'_{N-1}\boldsymbol{A}'_{N-2}\cdots\boldsymbol{A}'_{k+1}\boldsymbol{B}'_k \\ \boldsymbol{B}_{N-1} \triangleq \boldsymbol{B}'_{N-1} \end{cases} \tag{39}$$

Since the initial state $\boldsymbol{X}_1$ is fixed, $\mathrm{d}\boldsymbol{X}_1 = 0$ holds. Then, Eq. (38) can be simplified as

$$\mathrm{d}\boldsymbol{Y}_N = \sum_{k=1}^{N-1}\boldsymbol{B}_k\mathrm{d}\boldsymbol{U}_k \tag{40}$$

where $\boldsymbol{B}_k$ can be computed recursively as follows

$$\begin{cases} \boldsymbol{B}^0_{N-1} = \boldsymbol{I}_{12} \\ \boldsymbol{B}^0_k = \boldsymbol{B}^0_{k+1}\boldsymbol{A}'_{k+1} \\ \boldsymbol{B}_k = \boldsymbol{B}^0_k\boldsymbol{B}'_k \end{cases} \tag{41}$$

The updated control input series $\boldsymbol{U}_k, k = 1, 2, \ldots, N-1$ can be expressed as $\boldsymbol{U}_k = \boldsymbol{U}^{\mathrm{p}}_k - \mathrm{d}\boldsymbol{U}_k$. $\boldsymbol{U}^{\mathrm{p}}_k$ is the control input from the previous iteration. $\mathrm{d}\boldsymbol{U}_k$ is the corresponding correction for $\boldsymbol{U}^{\mathrm{p}}_k$. Then, the objective function J in Eq. (23) can be given by

$$J = \frac{1}{2}\sum_{k=1}^{N-1}(\boldsymbol{U}^{\mathrm{p}}_k - \mathrm{d}\boldsymbol{U}_k)^{\mathrm{T}}\boldsymbol{Q}_k(\boldsymbol{U}^{\mathrm{p}}_k - \mathrm{d}\boldsymbol{U}_k) \tag{42}$$

Eqs. (40) and (42) formulate an appropriate equality constrained static optimization problem. Using optimization theory and after some mathematical manipulations, the updated control at step k is obtained as[30]

$$\boldsymbol{U}_k = \boldsymbol{Q}_k^{-1}\boldsymbol{B}_k^{\mathrm{T}}\boldsymbol{A}_\lambda^{-1}(\mathrm{d}\boldsymbol{Y}_N - \boldsymbol{b}_\lambda), \quad k = 1, 2, \ldots, N-1 \tag{43}$$

where $\boldsymbol{A}_\lambda$ and $\boldsymbol{b}_\lambda$ are

$$\boldsymbol{A}_\lambda = -\sum_{k=1}^{N-1}\boldsymbol{B}_k\boldsymbol{Q}_k^{-1}\boldsymbol{B}_k^{\mathrm{T}} \tag{44}$$

$$\boldsymbol{b}_\lambda = \sum_{k=1}^{N-1}\boldsymbol{B}_k\boldsymbol{U}^{\mathrm{p}}_k \tag{45}$$

Eq. (43) is structurally similar to the original form which is not directly applicable. However, the new expressions in Eqs. (34) and (35) yield an applicable closed-form solution of the MPSP on SE(3). It can be used to obtain the fixed-finite-horizon energy sub-optimal control with hard terminal constraints for the 6-DOF spacecraft described on SE(3). $\mathrm{d}\boldsymbol{Y}_N$ is the predicted terminal output error between $\boldsymbol{Y}_N$ and $\boldsymbol{Y}_{\mathrm{d}}$, and its computation will be elaborated in the next section.

3.3. Definition of $\mathrm{d}\boldsymbol{Y}_N$

Considering the definition of $\boldsymbol{Y}_N$ in Eq. (22), $\mathrm{d}\boldsymbol{Y}_N$ is the predicted terminal error between $(\boldsymbol{g}_N, \boldsymbol{\xi}_N)$ and $(\boldsymbol{g}_{\mathrm{d}}, \boldsymbol{\xi}_{\mathrm{d}})$. $\boldsymbol{g}_N$ and $\boldsymbol{\xi}_N$are the normalized predicted terminal configuration and generalized velocity, respectively, which are obtained by the numerical integration of Eq. (16). Accordingly, $\boldsymbol{g}_{\mathrm{d}}$ and $\boldsymbol{\xi}_{\mathrm{d}}$ are the normalized desired configuration and generalized velocity, respectively. $\mathrm{d}\boldsymbol{Y}_N$ includes the configuration error $\boldsymbol{e}_{\boldsymbol{g}_N} \in \mathbf{R}^6$ and the generalized velocity error $\boldsymbol{e}_{\boldsymbol{\xi}_N} \in \mathbf{R}^6$, which can be expressed as

$$\mathrm{d}\boldsymbol{Y}_N = \begin{bmatrix} \boldsymbol{e}_{\boldsymbol{g}_N} \\ \boldsymbol{e}_{\boldsymbol{\xi}_N} \end{bmatrix} \tag{46}$$

With the given $(\boldsymbol{g}, \boldsymbol{\xi})$ and $(\boldsymbol{g}_{\mathrm{d}}, \boldsymbol{\xi}_{\mathrm{d}})$, the definitions and calculations of $\boldsymbol{e}_{\boldsymbol{g}}(\boldsymbol{g}, \boldsymbol{g}_{\mathrm{d}}) \in \mathbf{R}^6$ and $\boldsymbol{e}_{\boldsymbol{\xi}}(\boldsymbol{g}, \boldsymbol{\xi}, \boldsymbol{g}_{\mathrm{d}}, \boldsymbol{\xi}_{\mathrm{d}}) \in \mathbf{R}^6$ are elaborated in this subsection.

Since SE(3) is a Lig group, its compatible group operation and zero element are matrix multiplication and four-dimensional unit matrix $\boldsymbol{I}_{4\times4}$, respectively. Then, with the given configurations $\boldsymbol{g} \in \mathrm{SE}(3)$ and $\boldsymbol{g}_{\mathrm{d}} \in \mathrm{SO}(3)$, the group error $\boldsymbol{g}_{\mathrm{e}}$ between $\boldsymbol{g}$ and $\boldsymbol{g}_{\mathrm{d}}$ is defined as[17,18]

$$\boldsymbol{g}_{\mathrm{e}} \triangleq \boldsymbol{g}_{\mathrm{d}}^{-1}\boldsymbol{g} = \begin{bmatrix} \boldsymbol{R}_{\mathrm{d}}^{\mathrm{T}}\boldsymbol{R} & \boldsymbol{R}_{\mathrm{d}}^{\mathrm{T}}(\boldsymbol{p} - \boldsymbol{p}_{\mathrm{d}}) \\ 0_{1\times3} & 1 \end{bmatrix} \in \mathrm{SE}(3) \tag{47}$$

where, $\boldsymbol{g}_{\mathrm{e}}$ is the configuration tracking error from $\boldsymbol{g}$ to $\boldsymbol{g}_{\mathrm{d}}$. $\boldsymbol{g}_{\mathrm{e}} = \boldsymbol{I}_{4\times4}$ holds if and only if $\boldsymbol{g} = \boldsymbol{g}_{\mathrm{d}}$ is satisfied. Then, $\boldsymbol{e}_{\boldsymbol{g}}$ can be defined as the exponential coordinate of $\boldsymbol{g}_{\mathrm{e}}$ using the logarithm map $\log_{\mathrm{SE}(3)} : \mathrm{SE}(3) \to \mathrm{se}(3)$ as

$$\boldsymbol{e}_{\boldsymbol{g}} = \left(\log_{\mathrm{SE}(3)}\boldsymbol{g}_{\mathrm{e}}\right)^{\vee} \tag{48}$$

The inverse map of $\log_{\mathrm{SE}(3)}$ is the exponential map, which is $\exp_{\mathrm{SE}(3)} : \mathrm{se}(3) \to \mathrm{SE}(3)$. The calculations and definitions of the exponential and logarithm maps can be found in B. The exponential coordinate vector $\boldsymbol{e}_{\boldsymbol{g}}$ for the configuration tracking error $\boldsymbol{g}_{\mathrm{e}}$ can be also expressed as

$$\boldsymbol{e}_{\boldsymbol{g}} = \begin{bmatrix} \boldsymbol{e}_{\boldsymbol{R}} \\ \boldsymbol{e}_{\boldsymbol{p}} \end{bmatrix} \in \mathbf{R}^6 \tag{49}$$

where $\boldsymbol{e}_{\boldsymbol{R}} \in \mathbf{R}^3$ represents the attitude tracking error (attitude error vector), and $\boldsymbol{e}_{\boldsymbol{p}} \in \mathbf{R}^3$ represents the position tracking error (position error vector).

The generalized velocity error between $(\boldsymbol{g}, \boldsymbol{\xi})$ and $(\boldsymbol{g}_{\mathrm{d}}, \boldsymbol{\xi}_{\mathrm{d}})$ is defined as[18]

$$\begin{aligned} \boldsymbol{e}_{\boldsymbol{\xi}} &= \boldsymbol{\xi} - \mathrm{Ad}_{\boldsymbol{g}_{\mathrm{e}}^{-1}}\boldsymbol{\xi}_{\mathrm{d}} \\ &= \boldsymbol{\xi} - \mathrm{Ad}_{\boldsymbol{g}^{-1}\boldsymbol{g}_{\mathrm{d}}}\boldsymbol{\xi}_{\mathrm{d}} \end{aligned} \tag{50}$$

where $\mathrm{Ad}_{\boldsymbol{g}} : \mathbf{R}^6 \to \mathbf{R}^6$ is the adjoint map which transforms the generalized velocity in the desired B-Frame to the actual B-Frame. Moreover, $\mathrm{Ad}_{\boldsymbol{g}}\boldsymbol{X} = (\boldsymbol{g}\boldsymbol{X}^{\wedge}\boldsymbol{g}^{-1})^{\vee}$ holds for any given $\boldsymbol{X} \in \mathbf{R}^6$. $\mathrm{Ad}_{\boldsymbol{g}}$ can be also expressed in a matrix form, which is

$$\mathrm{Ad}_{\boldsymbol{g}} = \mathrm{Ad}_{(\boldsymbol{R},\boldsymbol{p})} = \begin{bmatrix} \boldsymbol{R} & 0 \\ \boldsymbol{p}^{\wedge}\boldsymbol{R} & \boldsymbol{R} \end{bmatrix} \tag{51}$$

Similar to Eq. (49), the generalized velocity error vector $\boldsymbol{e}_{\boldsymbol{\xi}}$ is given by

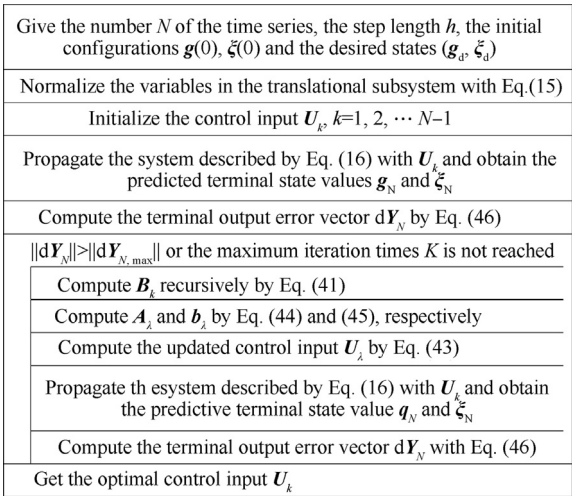

Fig. 2 Nassi Shneiderman diagram for the implementation of the MPSP on SE(3).

$$e_\xi = \begin{bmatrix} e_\Omega \\ e_V \end{bmatrix} \in \mathbf{R}^6 \tag{52}$$

where $e_\Omega \in \mathbf{R}^3$ and $e_V \in \mathbf{R}^3$ are the angular velocity error vector and the position velocity error vector, respectively.

With the predicted terminal states (g_N, ξ_N) and the desired states (g_d, ξ_d), the configuration error e_{g_N} and generalized velocity error e_{ξ_N} are calculated by Eq. (48) and Eq. (50), respectively. Then, dY_N in Eq. (46) is obtained.

To this point, the closed-form solution of the sub-optimal fixed-finite-horizon control on SE(3) is obtained based on the MPSP technique. The implementation steps of the proposed sub-optimal control scheme applied to the 6-DOF spacecraft modeled on SE(3) are displayed in Fig. 2. In order to limit the calculation time needed for iterations, the threshold $dY_{N,max}$ and the maximum iteration times K are used in Fig. 2. Therefor, the control scheme is sub-optimal when it is applied in practice.

In order to stabilize the configuration of a 6-DOF spacecraft considering system disturbance and state measurement errors, the proposed sub-optimal control scheme can be applied online in a shrinking horizon.[36] The control strategy is depicted in Fig. 3. The sub-optimal control input $U_k, k = 1, 2, \ldots, N-1$ is updated and computed online by the MPSP based on the measured states at every step between two executions. Moreover, t_{PH} represents the predicted horizon, which is diminishing over time, as t_f is fixed. In addition, t_k, $k = 1, 2, \ldots, N-1$ is the moment when the control input $U_k, k = 1, 2, \ldots, N-1$ is updated, and t_{EH} denotes the execution horizon.

4. Simulation

In this section, the results of applying the proposed method to control a rigid-body spacecraft modeled on SE(3) are simulated in a MATLAB environment. The proposed configuration control method is applied in an offline ideal scenario and an online practical scenario.

4.1. Offline results

In order to achieve the set-point maneuvers of a rigid-body spacecraft, the desired configuration of spacecraft is fixed as $g_d = I$. The attitude of rigid-body spacecraft is described by the exponential map $\exp_{SO(3)} : so(3) \to SO(3)$ as $R = \exp_{SO(3)}(x^\wedge)$, which is defined in Eq. (B1) in Appendix B. To illustrate the global expression of SO(3), $x(0)$ is set as $[-2.49, 1.49, -1.12]$ with $\|x(0)\| = 0.99\pi$, and the initial angular velocity $\Omega(0)$ is set as $[0, 0, 0]$. The initial position is set as $[-3.6, -3, 2]$, and the initial position velocity is set as $[0, 0, 0]$. The initial control input series is set to zero as $U_k^p = 0_{6\times1}, k = 1, 2, \ldots, N-1$. Disturbances and uncertainties are not considered in this section.

The mass of spacecraft is set as 56.7 kg, and the inertial matrix is set as[4,6]

$$J = \begin{bmatrix} 4.85 & 0 & 0 \\ 0 & 5.10 & 0 \\ 0 & 0 & 4.76 \end{bmatrix} \text{kg} \cdot \text{m}^2$$

The control parameters used are set as those in Table 1. The simulation results are depicted in Figs. 4–6.

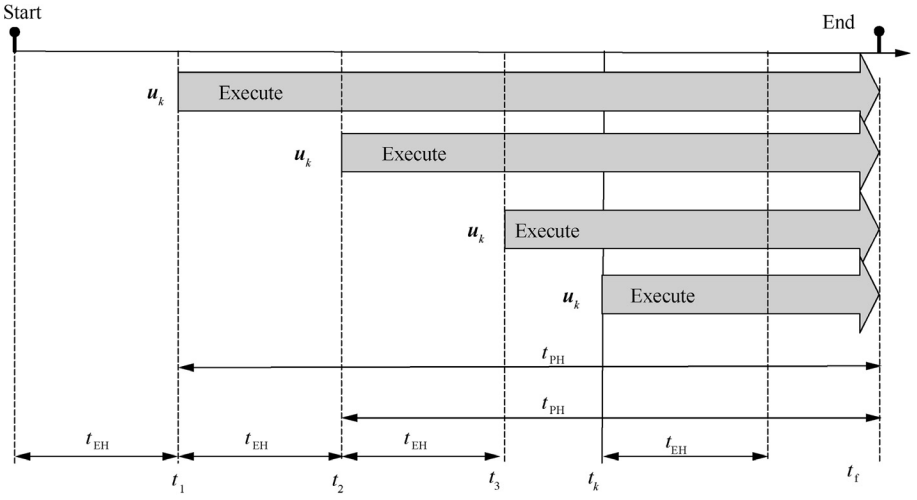

Fig. 3 Control strategy of the shrinking horizon control [36].

Table 1 Control parameters.

Parameters	Values	Parameters	Values
T (s)	10	h (s)	0.1
N	1000	$\mathrm{d}\boldsymbol{Y}_{\max}$	10^{-3}
p_{m}(m)	8	V_{m} (m·s^{-1})	8
K	20		

Fig. 4(a) shows the configuration error vector $\boldsymbol{e}_{\boldsymbol{g}}$ changing versus time. It can be seen from Fig. 4(a) and Fig. 4(b) that the attitude error vector $\boldsymbol{e}_{\boldsymbol{R}}$ and the position error vector $\boldsymbol{e}_{\boldsymbol{p}}$ converge to zero at the scheduled time $t_{\mathrm{f}} = 10$ s.

Fig. 5 depicts the generalized velocity error vector $\boldsymbol{e}_{\xi}$ changing with time. Fig. 5(a) and Fig. 5(b) show that the angular error vector $\boldsymbol{e}_{\Omega}$ and the position velocity error vector $\boldsymbol{e}_{\boldsymbol{V}}$ converge to zero at $t_{\mathrm{f}} = 10$ s. Combined with the results in Fig. 4, it can be concluded that the expected set-point manoeuvres can be achieved for rigid-body spacecraft.

Fig. 6 depicts the time histories of the optimal control input $\boldsymbol{U}$. Fig. 6(a) and Fig. 6(b) show the torque and force of 6-DOF spacecraft changing versus time, respectively.

The simulation results for different initial states are summarized in Table 2. It can be seen that the high accuracy is obtained for the configuration control of spacecraft using the proposed method.

For comparison, the Geometric Proportional-Derivative (GPD) controller designed in Ref. 18 are also simulated in the three cases. The simulation results of the three cases under the GPD are summarized in Table 3. It can be seen that the higher accuracy and less energy cost can be achieved by the MPSP compared with the GPD in Ref. 18.

4.2. Online results

To demonstrate the practical significance, the generalized external disturbance and state measurement errors of spacecraft are introduced. In addition, the MPSP is applied online to stabilize the configuration. In this subsection, combined with the shrinking horizon control, the numerical simulation of the online MPSP are carried out to illustrate its effectiveness.

The disturbance torque of spacecraft is set as[36,41]

$$\boldsymbol{d}_{\Omega}(t) = [0.2\sin(0.1t), -0.2\cos(0.2t), -0.2\sin(0.2t)]^{\mathrm{T}}\mathrm{N}\cdot\mathrm{m}$$

The disturbance force of spacecraft is considered as

$$\boldsymbol{d}_{\boldsymbol{V}}(t) = [-0.3\sin(0.1t), 0.3\cos(0.2t), 0.3\sin(0.2t)]^{\mathrm{T}}\mathrm{N}$$

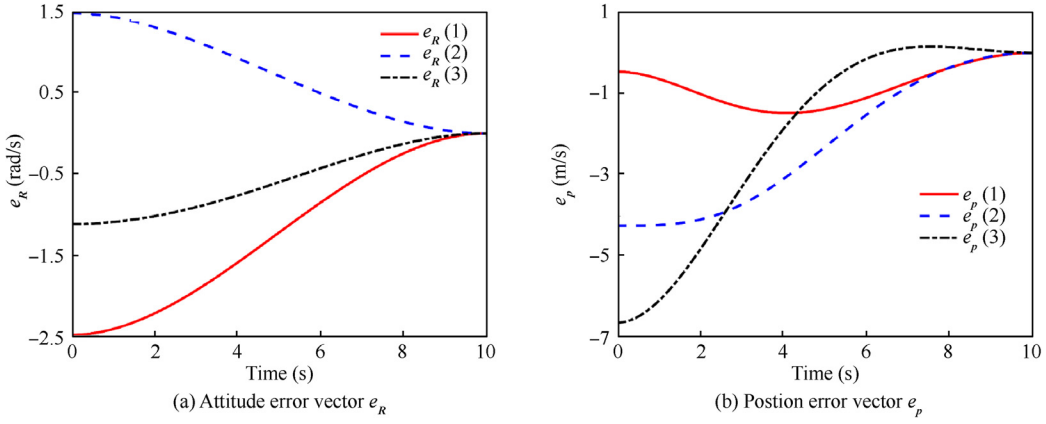

(a) Attitude error vector e_R (b) Postion error vector e_p

Fig. 4 Offline: Configuration error vector $\boldsymbol{e}_{\boldsymbol{g}}$ changing versus time.

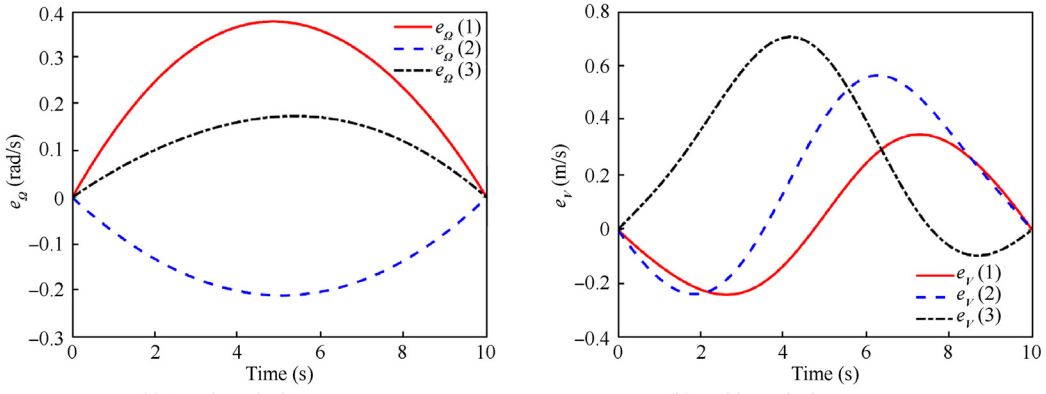

(a) Angular velocity error vector e_Ω (b) Position velocity error vector e_V

Fig. 5 Offline: Generalized velocity error vector $\boldsymbol{e}_{\xi}$ changing versus time.

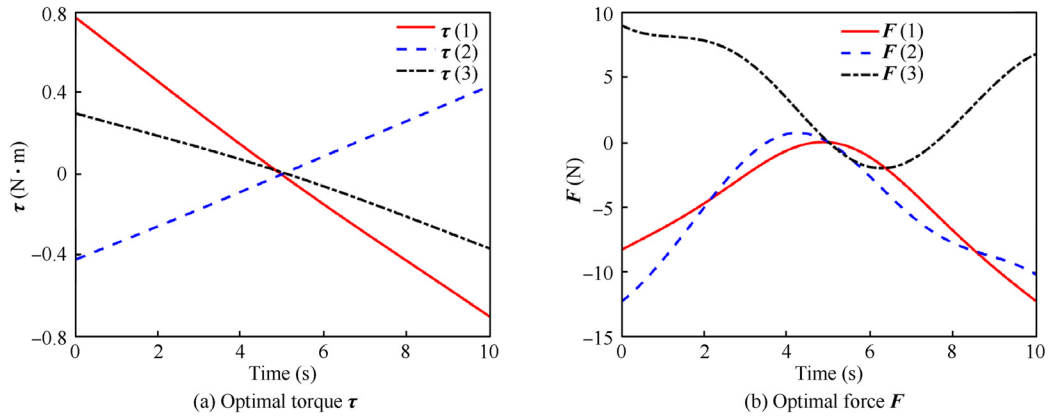

(a) Optimal torque $\boldsymbol{\tau}$ (b) Optimal force $\boldsymbol{F}$

Fig. 6 Offline: Optimal control input $\boldsymbol{U}$ changing versus time.

Table 2 Initial states and results of simulation.

Items	Variables	Case 1	Case 2	Case 3
Initial states	$\boldsymbol{x}(0)$ (rad)	$[-2.5, 1.5, -1.1]$	$[1.1, -0.9, 1.2]$	$[0.68, 1.51, -0.90]$
	$\boldsymbol{p}(0)$ (m)	$[-3.6, -3.0, 2.0]$	$[1.8, -1.5, 1]$	$[-0.6, 0.8, 1]$
	$\boldsymbol{\Omega}(0)$ (rad/s)	$[0, 0, 0]$	$[0, 0, 0]$	$[0, 0, 0]$
	$\boldsymbol{V}(0)$ (m/s)	$[0, 0, 0]$	$[0, 0, 0]$	$[0, 0, 0]$
Energy cost	J	876.6386	438.6018	244.6617
Accuracy	$\|\mathrm{d}\boldsymbol{Y}_N\|$	7.8895×10^{-4}	6.8845e-05	2.9005e-05
	$\left\|\boldsymbol{e}_{\boldsymbol{g}}^N\right\|$	1.7567×10^{-4}	5.2512e-05	1.7602e-05
	$\left\|\boldsymbol{e}_{\xi}^N\right\|$	7.6495×10^{-4}	4.1674e-05	2.2637e-05
Iteration		8	6	5
Computational time (s)		0.282	0.207	0.168

Table 3 Simulation results of GPD.

Items	Variables	Case 1	Case 2	Case 3
Energy cost	J	3.5773×10^{3}	854.3614	672.0488
Accuracy	$\|\mathrm{d}\boldsymbol{Y}_N\|$	0.3275	0.0621	0.0583
	$\left\|\boldsymbol{e}_{\boldsymbol{g}}^N\right\|$	0.0513	0.0311	0.0310
	$\left\|\boldsymbol{e}_{\xi}^N\right\|$	0.2719	0.0467	0.0407

The measurement error of attitude is expressed by the exponential map of SO(3) in Eq. (B1) in Appendix B. The relationships between the observed states $\hat{\boldsymbol{R}}, \hat{\boldsymbol{p}}, \hat{\boldsymbol{\Omega}}, \hat{\boldsymbol{V}}$ and the actual states $\boldsymbol{R}, \boldsymbol{p}, \boldsymbol{\Omega}, \boldsymbol{V}$ are described as

$$\begin{cases} \hat{\boldsymbol{R}} & = \boldsymbol{R} * \exp(\boldsymbol{\sigma}_1{}^{\wedge}) \\ \hat{\boldsymbol{p}} & = \boldsymbol{p} + \boldsymbol{\sigma}_2 \\ \hat{\boldsymbol{\Omega}} & = \boldsymbol{\Omega} + \boldsymbol{\sigma}_3 \\ \hat{\boldsymbol{V}} & = \boldsymbol{V} + \boldsymbol{\sigma}_4 \end{cases} \tag{53}$$

where $\boldsymbol{\sigma}_j \in \mathbf{R}^3, j = 1, 2, 3, 4$ are the measurement errors of states. $\boldsymbol{\sigma}_j$ are the Gaussian noise and satisfy $\boldsymbol{\sigma}_j(i) \sim N(0, 0.003)$, $i = 1, 2, 3$.

The control parameters for the online application are set as follows. The initial length of the shrinking horizon is set as $t_{\mathrm{PH}} = 10$ s. The execution horizon t_{EH} is 0.1s. The control parameters of the MPSP, the initial and desired states are set the same as those of Case 1 in Section 4.1. The simulation results of the close-loop system are shown in Figs. 7–10.

The configuration error vector $\boldsymbol{e}_{\boldsymbol{g}}$ under the online MPSP changing versus time is depicted in Fig. 7. The time histories of the generalized velocity error vector $\boldsymbol{e}_{\xi}$ are shown in Fig. 8. The simulation results in Figs. 7 and 8 demonstrate that the error vectors $\boldsymbol{e}_{\boldsymbol{g}}$ and $\boldsymbol{e}_{\xi}$ of the closed-loop spacecraft system under the online MPSP converge to zero in scheduled time $t_{\mathrm{f}} = 10$ s, while disturbances and measurement errors exist.

Fig. 9 shows the time histories of the torque $\boldsymbol{\tau}$ and the force $\boldsymbol{F}$ of the closed-loop spacecraft system. Compared with the simulation results of the offline MPSP in Fig. 6, there are some jitters for the generalized force input in Fig. 9, because of the Gaussian noises of the measured states in Eq. (53). However, the jitters only become noticeable in the terminal period. As the shrinking horizon control strategy is applied here, the length of t_{PH} decreases to a small value at the terminal stage.

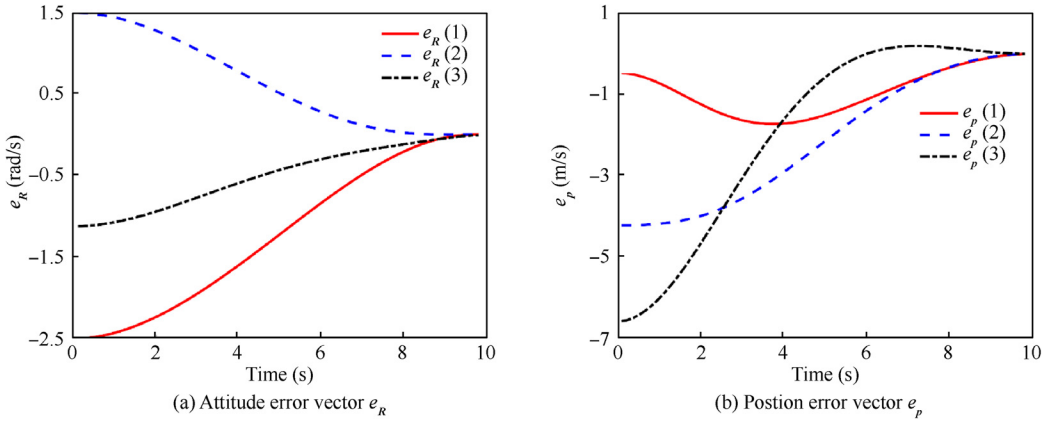

Fig. 7 Online: Configuration error vector e_g changing with time.

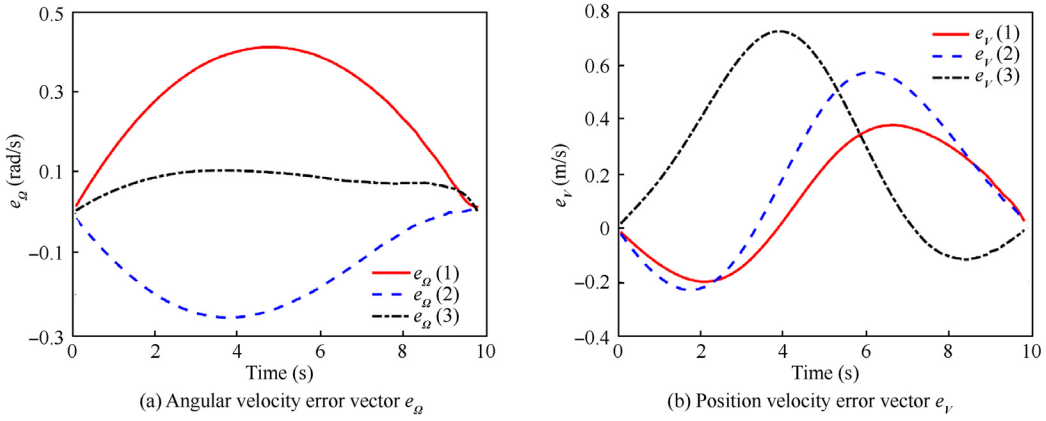

Fig. 8 Online: Generalized velocity error vector e_ξ changing with time.

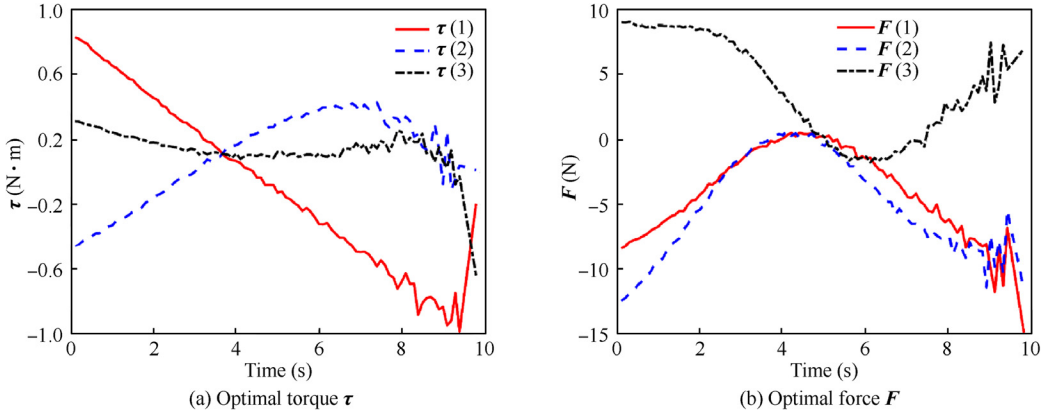

Fig. 9 Online: Optimal control input U changing with time.

In this period, the same level of disturbances and measurement errors cause more visible changes for optimal control histories.

Fig. 10 demonstrates the configuration trajectory of rigid-body spacecraft changing with time. The spacecraft's position and the orientation of the body-fixed frame are plotted along the trajectory at 0, 2, 4, 6, 8, 10 s, respectively. The configuration of the rigid-body spacecraft controlled by the online MPSP can be stabilized to the desired configuration at the scheduled time $t_f = 10$ s with a high efficiency (without overshot). It can also be seen that the large-angle maneuver (greater than $\pi/2$) can be also achieved without singularity and unwinding phenomena.

It can be seen from Table 2 that the computation time of the offline MPSP in a MATLAB environment is longer than the execution horizon $t_{EH} = 0.1$s of the online MPSP. However, when the MPSP is applied online, the control series can

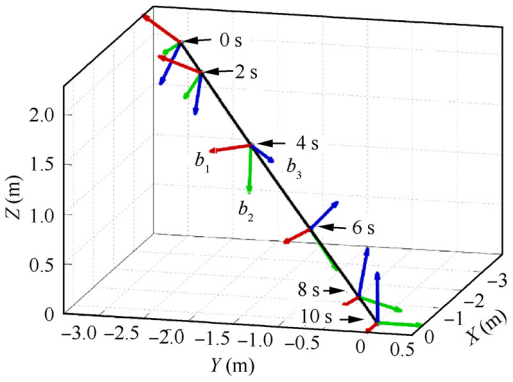

Fig. 10 Configuration trajectory of spacecraft under the online MPSP.

be iterated and updated based on the results of the previous step. Therefore, the computation time can be significantly shortened and less than $t_{\mathrm{EH}} = 0.1$s, Therefore, the MPSP can be applied online in practice.

5. Conclusions

This paper addresses the sub-optimal fixed-finite-horizon spacecraft configuration control on SE(3) based on the Model Predictive Static Programming (MPSP). The translational dynamical equations are normalized to ensure a similar numerical range for the translational and rotational subsystems of 6-DOF spacecraft. Then, using the variational principle and the geometric property of Lie group, the states' variation is expressed by an explicit discrete-time form in an Euclidean space, which can be integrated with the MPSP to control the configuration on SE(3) in a fixed horizon. The geometric sub-optimal control leads to promising simulation results with a high accuracy. Moreover, the simulation results of the online application with disturbances and errors demonstrate that the proposed sub-optimal method can stabilize the configuration of a 6-DOF spacecraft in practical scenarios.

Declaration of Competing Interest

The authors declare that they have no known competing financial interests or personal relationships that could have appeared to influence the work reported in this paper.

Acknowledgment

Haichao Hong acknowledges the support of the TUM University Foundation Fellowship.

Appendix A. Model predictive static programming design

In this section, the brief summary of the MPSP are introduced, which can be applied to a nonlinear dynamical system modeled on an Euclidean space. For more details about the MPSP, readers can refer to Refs. 30,31.

To begin, a general nonlinear dynamical system is considered here in a discrete-time form. Its state and output dynamics are given by

$$\boldsymbol{X}_{k+1} = \boldsymbol{F}_k(\boldsymbol{X}_k, \boldsymbol{U}_k) \tag{A1}$$

$$\boldsymbol{Y}_k = \boldsymbol{h}_k(\boldsymbol{X}_k) \tag{A2}$$

where $\boldsymbol{X}_k \in \mathbf{R}^n$ is the state vector. $\boldsymbol{U}_k \in \mathbf{R}^m$ is the input vector. $\boldsymbol{Y}_k \in \mathbf{R}^p$ is the output vector. $k = 1, 2, \ldots, N$ are the time steps. The primary objective of this method is to obtain a suitable control input $\boldsymbol{U}_k, k = 1, 2, \ldots, N-1$ to let the terminal output $\boldsymbol{Y}_N$ go to a desired value $\boldsymbol{Y}_{\mathrm{d}}$, i.e., $\boldsymbol{Y}_N \to \boldsymbol{Y}_{\mathrm{d}}$, with minimum control effort.

As $\boldsymbol{Y}_N$ and $\boldsymbol{Y}_{\mathrm{d}}$ belong to a flat Euclidean space $\mathbf{R}^p$, The error between $\boldsymbol{Y}_N$ and $\boldsymbol{Y}_{\mathrm{d}}$ is denoted and calculated by $\Delta\boldsymbol{Y}_N = \boldsymbol{Y}_N - \boldsymbol{Y}_{\mathrm{d}}$. When $\|\Delta\boldsymbol{Y}_N\|$is small, $\boldsymbol{Y}_N$ can be expanded and approximated about $\boldsymbol{Y}_{\mathrm{d}}$ using Taylor series expansion. Neglecting the higher order terms, $\Delta\boldsymbol{Y}_N$ can be written as

$$\Delta\boldsymbol{Y}_N \cong \mathrm{d}\boldsymbol{Y}_N = \left[\frac{\partial \boldsymbol{Y}_N}{\partial \boldsymbol{X}_N}\right]\mathrm{d}\boldsymbol{X}_N \tag{A3}$$

From Eq. (A1), the small error in state at step $k+1$ can be deduced and represented by the small errors in state and control at step k, which is

$$\mathrm{d}\boldsymbol{X}_{k+1} = \left[\frac{\partial \boldsymbol{F}_k}{\partial \boldsymbol{X}_k}\right]\mathrm{d}\boldsymbol{X}_k + \left[\frac{\partial \boldsymbol{F}_k}{\partial \boldsymbol{U}_k}\right]\mathrm{d}\boldsymbol{U}_k \tag{A4}$$

Combined with $\mathrm{d}\boldsymbol{X}_k$ expressed in Eq. (A4), $\mathrm{d}\boldsymbol{Y}_N$ in Eq. (A3) is expanded as

$$\mathrm{d}\boldsymbol{Y}_N = \left[\frac{\partial \boldsymbol{Y}_N}{\partial \boldsymbol{X}_N}\right]\left(\left[\frac{\partial \boldsymbol{F}_{N-1}}{\partial \boldsymbol{X}_{N-1}}\right]\mathrm{d}\boldsymbol{X}_{N-1} + \left[\frac{\partial \boldsymbol{F}_{N-1}}{\partial \boldsymbol{U}_{N-1}}\right]\mathrm{d}\boldsymbol{U}_{N-1}\right) \tag{A5}$$

Similarly, $\mathrm{d}\boldsymbol{X}_{N-1}$ can be expressed by the small error vectors in state and control at step $N-2$. Repeating this process until $k = 1$, $\mathrm{d}\boldsymbol{Y}_N$ can be expanded as

$$\mathrm{d}\boldsymbol{Y}_N = \boldsymbol{A}\mathrm{d}\boldsymbol{X}_1 + \boldsymbol{B}_1\mathrm{d}\boldsymbol{U}_1 + \boldsymbol{B}_2\mathrm{d}\boldsymbol{U}_2 + \cdots + \boldsymbol{B}_{N-1}\mathrm{d}\boldsymbol{U}_{N-1} \tag{A6}$$

where $\boldsymbol{A} \in \mathbf{R}^{n\times n}, \boldsymbol{B}_k \in \mathbf{R}^{n\times p}, k = 1, 2, \ldots, N-2$ are calculated by

$$\begin{cases} \boldsymbol{A} \triangleq \left[\frac{\partial \boldsymbol{Y}_N}{\partial \boldsymbol{X}_N}\right]\left[\frac{\partial \boldsymbol{F}_{N-1}}{\partial \boldsymbol{X}_{N-1}}\right]\cdots\left[\frac{\partial \boldsymbol{F}_1}{\partial \boldsymbol{X}_1}\right] \\ \boldsymbol{B}_k \triangleq \left[\frac{\partial \boldsymbol{Y}_N}{\partial \boldsymbol{X}_N}\right]\left[\frac{\partial \boldsymbol{F}_{N-1}}{\partial \boldsymbol{X}_{N-1}}\right]\cdots\left[\frac{\partial \boldsymbol{F}_{k+1}}{\partial \boldsymbol{X}_{k+1}}\right]\left[\frac{\partial \boldsymbol{F}_k}{\partial \boldsymbol{U}_k}\right] \\ \boldsymbol{B}_{N-1} \triangleq \left[\frac{\partial \boldsymbol{Y}_N}{\partial \boldsymbol{X}_N}\right]\left[\frac{\partial \boldsymbol{F}_{N-1}}{\partial \boldsymbol{U}_{N-1}}\right]. \end{cases} \tag{A7}$$

$\boldsymbol{B}_k$ can be computed recursively as

$$\begin{cases} \boldsymbol{B}_{N-1}^0 = \left[\frac{\partial \boldsymbol{Y}_N}{\partial \boldsymbol{X}_N}\right] \\ \boldsymbol{B}_k^0 = \boldsymbol{B}_{k+1}^0\left[\frac{\partial \boldsymbol{F}_{k+1}}{\partial \boldsymbol{X}_{k+1}}\right] \\ \boldsymbol{B}_k = \boldsymbol{B}_k^0\left[\frac{\partial \boldsymbol{F}_k}{\partial \boldsymbol{U}_k}\right] \end{cases} \tag{A8}$$

Since the initial condition of state is fixed, $\mathrm{d}\boldsymbol{X}_1 = 0$ holds. Then, Eq. (A6) is further written as

$$\begin{aligned} \mathrm{d}\boldsymbol{Y}_N &= \boldsymbol{B}_1\mathrm{d}\boldsymbol{U}_1 + \boldsymbol{B}_2\mathrm{d}\boldsymbol{U}_2 + \cdots + \boldsymbol{B}_{N-1}\mathrm{d}\boldsymbol{U}_{N-1} \\ &= \sum_{k=1}^{N-1}\boldsymbol{B}_k\mathrm{d}\boldsymbol{U}_k \end{aligned} \tag{A9}$$

In Eq. (A9), there are $(N-1)m$ unknown variables and p linear equality constraints. Since $p < (N-1)m$, the system described by Eq. (A9) is under-constrained. In order to obtain its unique solution, some additional objectives should be introduced. Such as minimizing the following objective (cost) function

$$J=\frac{1}{2}\sum_{k=1}^{N-1}(\boldsymbol{U}_k^{\mathrm{p}}-\mathrm{d}\boldsymbol{U}_k)^{\mathrm{T}}\boldsymbol{Q}_k(\boldsymbol{U}_k^{\mathrm{p}}-\mathrm{d}\boldsymbol{U}_k) \tag{A10}$$

where $\boldsymbol{U}_k^{\mathrm{p}}, k=1,2,\ldots,N-1$ is the control input series obtained from the previous iteration. $\mathrm{d}\boldsymbol{U}_k$ is the corresponding correction for $\boldsymbol{U}_k^{\mathrm{p}}$. $\boldsymbol{U}_k=\boldsymbol{U}_k^{\mathrm{p}}-\mathrm{d}\boldsymbol{U}_k$ is the updated control input. $\boldsymbol{Q}_k\in\mathbf{R}^{m\times m}$ is the weight matrix, which is positive definite and chosen judiciously by the designer. Eqs. (A9) and (A10) formulate an equality constrained static optimization problem. Using optimization theory and after some mathematical manipulations, the updated control input at step k is given from Refs.[30,31] as

$$\boldsymbol{U}_k=\boldsymbol{Q}_k^{-1}\boldsymbol{B}_k^{\mathrm{T}}\boldsymbol{A}_\lambda^{-1}(\Delta\boldsymbol{Y}_N-\boldsymbol{b}_\lambda) \tag{A11}$$

where $\boldsymbol{A}_\lambda$ and $\boldsymbol{b}_\lambda$ are calculated as

$$\boldsymbol{A}_\lambda=-\sum_{k=1}^{N-1}\boldsymbol{B}_k\boldsymbol{Q}_k^{-1}\boldsymbol{B}_k^{\mathrm{T}} \tag{A12}$$

$$\boldsymbol{b}_\lambda=\sum_{k=1}^{N-1}\boldsymbol{B}_k\boldsymbol{U}_k^{\mathrm{p}} \tag{A13}$$

Now, the closed-form solution of the MPSP in an Euclidean space $\mathbf{R}^n$ is obtained. The MPSP can be used to solve the optimization problem with an explicit discrete-time nonlinear dynamical system like Eqs. (A1) and (A2).

Appendix B. Exponential and logarithmic map

For the Lie groups SO(3) and SE(3), with their Lie algebra so(3) and se(3), the exponential and logarithmic map is defined below[17].

Lemma B1. [Exponential Map] Given any Lie algebra $\hat{\boldsymbol{x}}\in\mathrm{so}(3)$ and $\bar{\boldsymbol{X}}=(\hat{\boldsymbol{x}},\boldsymbol{y})\in\mathrm{se}(3)$, the exponential map on $\mathrm{so}(3),\exp_{\mathrm{SO}(3)}:\mathrm{so}(3)\to\mathrm{SO}(3)$, and the exponential map on $\mathrm{se}(3),\exp_{\mathrm{SE}(3)}:\mathrm{se}(3)\to\mathrm{SE}(3)$ are defined as

$$\begin{cases}\exp_{\mathrm{SO}(3)}(\hat{\boldsymbol{x}}) &= \boldsymbol{I}+\frac{\sin\|\boldsymbol{x}\|}{\|\boldsymbol{x}\|}\hat{\boldsymbol{x}}+\frac{1-\cos\|\boldsymbol{x}\|}{\|\boldsymbol{x}\|^2}\hat{\boldsymbol{x}}^2\\ \exp_{\mathrm{SE}(3)}(\bar{\boldsymbol{X}}) &= \begin{bmatrix}\exp_{\mathrm{SO}(3)}(\hat{\boldsymbol{x}}) & \boldsymbol{A}(\boldsymbol{x})\boldsymbol{y}\\ 0 & 1\end{bmatrix}\end{cases} \tag{B1}$$

where $\|\cdot\|$is the standard Euclidean norm. Matrix $\boldsymbol{A}(\boldsymbol{x})$ is expressed as

$$\boldsymbol{A}(\boldsymbol{x})=\boldsymbol{I}_3+\left(\frac{1-\cos\|\boldsymbol{x}\|}{\|\boldsymbol{x}\|}\right)\frac{\hat{\boldsymbol{x}}}{\|\boldsymbol{x}\|}+\left(1-\frac{\sin\|\boldsymbol{x}\|}{\hat{\boldsymbol{x}}}\right)\frac{\hat{\boldsymbol{x}}^2}{\|\boldsymbol{x}\|^2} \tag{B2}$$

Eq. (B1) is the Rodrigues' formula. $\|\boldsymbol{x}\|<\pi$ and $\frac{\boldsymbol{x}}{\|\boldsymbol{x}\|}$ represent the rotation angle and axis between $\boldsymbol{R}$ and $\boldsymbol{I}_3$, respectively. $\boldsymbol{x}\in\mathbf{R}^3,[\boldsymbol{x}^{\mathrm{T}}\quad\boldsymbol{y}^{\mathrm{T}}]^{\mathrm{T}}$ are the exponential coordinates of Lie groups SO(3), SE(3), respectively.

The inverse map of exponential map is logarithmic map, whose definition is given as follows.

Lemma B2. For any given $\boldsymbol{R}\in\mathrm{SO}(3)$ and $(\boldsymbol{R},\boldsymbol{p})\in\mathrm{SE}(3)$ with $\mathrm{tr}(\boldsymbol{R})\neq-1$ holding for $\boldsymbol{R}$, the logarithmic maps on $\mathrm{SO}(3),\log_{\mathrm{SO}(3)}:\mathrm{SO}(3)\to\mathrm{so}(3)$, and on $\mathrm{SE}(3),\log_{\mathrm{SE}(3)}:\mathrm{SE}(3)\to\mathrm{se}(3)$, are defined as

$$\begin{cases}\log_{\mathrm{SO}(3)}(\boldsymbol{R}) &= \frac{\Phi}{2\sin\Phi}(\boldsymbol{R}-\boldsymbol{R}^{\mathrm{T}})\\ \log_{\mathrm{SE}(3)}(\boldsymbol{R},\boldsymbol{p}) &= \begin{bmatrix}\boldsymbol{x} & \boldsymbol{A}^{-1}(\boldsymbol{x})\boldsymbol{y}\\ 0 & 1\end{bmatrix}\end{cases} \tag{B3}$$

where $\cos\Phi=\frac{1}{2}[\mathrm{tr}(\boldsymbol{R})-1]$ is satisfied for Φ. Since $\mathrm{tr}(\boldsymbol{R})\neq-1$ is satisfied for $\boldsymbol{R},|\Phi|<\pi$ always holds. Define variable $\boldsymbol{x}$ with $\hat{\boldsymbol{x}}=\log_{\mathrm{SO}(3)}(\boldsymbol{R})$. Then, the expression of $\boldsymbol{A}^{-1}(\boldsymbol{x})$ is

$$\boldsymbol{A}^{-1}(\boldsymbol{x})=\boldsymbol{I}_3-\frac{1}{2}\hat{\boldsymbol{x}}+\left(1-\frac{\|\boldsymbol{x}\|}{2}\cot\left(\frac{\|\boldsymbol{x}\|}{2}\right)\right)\frac{\hat{\boldsymbol{x}}^2}{\|\boldsymbol{x}\|^2} \tag{B4}$$

References

1. Hu QL, Xiao L, Wang CL. Adaptive fault-tolerant attitude tracking control for spacecraft with time-varying inertia uncertainties. *Chin J Aeronaut* 2019;**32**(3):674–87.
2. Yue XK, Xue XH, Wen HW, et al. Adaptive control for attitude coordination of leader-following rigid spacecraft systems with inertia parameter uncertainties. *Chin J Aeronaut* 2019;**32**(3):688–700.
3. Chen LM, Li CJ, Guo YN, et al. Spacecraft formation-containment flying control with time-varying translational velocity. *Chin J Aeronaut* 2020;**33**(1):271–81.
4. Lee D, Vukovich G. Robust adaptive terminal sliding mode control on SE(3) for autonomous spacecraft rendezvous and docking. *Nonlinear Dyn* 2016;**83**(4):2263–79.
5. Sanyal A, Holguin L, Viswanathan SP. Guidance and control for spacecraft autonomous chasing and close proximity maneuvers. *IFAC Proc* 2012;**45**(13):753–8.
6. Lee D, Sanyal AK, Butcher EA, et al. Finite-time control for spacecraft body-fixed hovering over an asteroid. *IEEE Trans Aerosp Electron Syst* 2015;**51**(1):506–20.
7. Lee D, Sanyal AK, Butcher EA, et al. Almost global asymptotic tracking control for spacecraft body-fixed hovering over an asteroid. *Aerosp Sci Technol* 2014;**38**:105–15.
8. Lee D, Vukovich G. Adaptive sliding mode control for spacecraft body-fixed hovering in the proximity of an asteroid. *Aerosp Sci Technol* 2015;**46**:471–83.
9. Sun C, Yuan JP, Zhu ZX. Neural adaptive control for a ground experiment of the space proximity operation in a six-degree-of-freedom micro-gravity simulation system. *Chin J Aeronaut* 2020;**33**(9):2420–33.
10. Lee D, Butcher EA, Sanyal AK. Sliding mode control for decentralized spacecraft formation flying using geometric mechanics. *Adv Astron Sci* 2014;**150**:3149–68.
11. Lee D, Sanyal AK, Butcher EA. Asymptotic tracking control for spacecraft formation flying with decentralized collision avoidance. *J Guid Control Dyn* 2015;**38**(4):587–600.
12. Nazari M, Butcher EA, Yucelen T, et al. Decentralized consensus control of a rigid-body spacecraft formation with communication delay. *J Guid Control Dyn* 2016;**39**(4):838–51.
13. Ye D, Zhang JQ, Sun ZW. Extended state observer-based finite-time controller design for coupled spacecraft formation with actuator saturation. *Adv Mech Eng* 2017;**9**(4):1–17.
14. Singla P, Subbarao K, Junkins JL. Adaptive output feedback control for spacecraft rendezvous and docking under measurement uncertainty. *J Guid Control Dyn* 2006;**29**(4):892–902.
15. Lee D, Cochran Jr JE, No TS. Robust position and attitude control for spacecraft formation flying. *J Aerosp Eng* 2012;**25**(3):436–47.
16. Park HE, Park SY, Park C, et al. Development of integrated orbit and attitude software-in-the-loop simulator for satellite formation flying. *J Astron Space Sci* 2013;**30**:1–10.
17. Bullo F, Murray RM. Proportional Derivative (PD) control on the Euclidean Group. *European control conference* 1995;1091–7.

18. Bullo F, Murray RM. Tracking for fully actuated mechanical systems: a geometric framework. *Automatica* 1999;**35**(1):17–34.
19. Wang YL, Hong HC, Guo J, et al. Configuration error function design and application to fixed-time geometric terminal sliding-mode control on SE(3). *Acta Astronaut* 2020;**174**:61–71.
20. Starek JA, Kolmanovsky IV. Nonlinear model predictive control strategy for low thrust spacecraft missions. *Optim Control Appl Methods* 2014;**35**(1):1–20.
21. Di Cairano S, Doering J, Kolmanovsky IV, et al. Model predictive control of engine speed during vehicle deceleration. *IEEE Trans Control Syst Technol* 2014(22);2205–17.
22. Kalabić U, Gupta R, Di Cairano S, et al. MPC on manifolds with an application to the control of spacecraft attitude on SO(3). *Automatica* 2017;**76**:293–300.
23. Kalabić U, Gupta R, Di Cairano S, et al. Constrained spacecraft attitude control on SO(3) using reference governors and nonlinear model predictive control. *2014 American control conference*. 2014 June 4-6; Portland, OR, USA. Piscataway: IEEE Press; 2014. p.5586-93.
24. Kalabić U, Gupta R, Di Cairano S, et al. MPC on Manifolds with an Application to SE(3). *2016 American control conference*. 2016 July 6-8; Boston, MA, USA. Piscataway: IEEE Press; 2016.p.7-12.
25. Lee T, McClamroch NH, Leok M. Optimal control of a rigid body using geometrically exact computations on SE(3). *Proceedings of the 45th IEEE conference on decision and control. 2006 December 13-15; San Diego, CA, USA*. Piscataway: IEEE Press; 2006. p. 2710–5.
26. Hussein II. Motion planning for multi-spacecraft interferometric imaging systems[dissertation]. Michigan: The University of Michigan; 2005.
27. Craioveanu M, Pop C, Aron A, et al. An optimal control problem on the special Euclidean group SE(3, R). *International conference differential geometry-dynamical systems;* 2009. p. 68–78.
28. Liu YF, Geng ZY. Finite-time optimal formation control of multi-agent systems on the Lie group SE(3). *Int J Control* 2013;**86**(10):1675–86.
29. Werbos PJ. Approximate dynamic programming for real-time control and neural modeling. *Handbook of intelligent control neural fuzzy and adaptive approaches*. New York: Van Nostrand Reinhold; 1992. p. 493–526.
30. Padhi R, Kothari M. Model predictive static programming: a computationally efficient technique for suboptimal control design. *Int J Innov Comput, Inform Control* 2009;**5**(2):399–411.
31. Oza HB, Padhi R. Impact-angle-constrained suboptimal model predictive static programming guidance of air-to-ground missiles. *J Guid Control Dyn* 2012;**35**(1):153–64.
32. Maity A, Oza HB, Padhi R. Generalized model predictive static programming and angle-constrained guidance of air-to-ground missiles. *J Guid Control Dyn* 2014;**37**(6):1897–913.
33. Hong HC, Maity A, Holzapfel F, et al. Adaptive trajectory generation based on real-time estimated parameters for impaired aircraft landing. *Int J Syst Sci* 2019;**50**(15):2733–51.
34. Tavakoli F, Novinzadeh AB. Designing a closed-loop guidance system to increase the accuracy of satellite-carrier boosters' landing point. *Aerosp Sci Technol* 2018;**76**:242–9.
35. Banerjee A, Padhi R, Vatsal V. Optimal guidance for accurate lunar soft landing with minimum fuel consumption using model predictive static programming. *2015 American control conference*. 2015 July 1-3; Chicago, IL, USA. Piscataway: IEEE Press; 2015. p.1861-6.
36. Wang YL, Hong HC, Tang SJ. Geometric control with model predictive static programming on SO(3). *Acta Astronaut* 2019;**159**:471–9.
37. Nordkvist N, Sanyal AK. A Lie group variational integrator for rigid body motion in SE(3) with applications to underwater vehicle dynamics. *49th IEEE conference on decision and control*. 2010 December 15-17; Atlanta, GA, USA. Piscataway: IEEE Press; 2010.p.5414-9.
38. Lee T, Leok M, Mcclamroch NH. Optimal attitude control of a rigid body using geometrically exact computations on SO(3). *J Dyn Control Syst* 2008;**14**(4):465–87.
39. Sreenath K, Lee T, Kumar V. Geometric control and differential flatness of a quadrotor UAV with a cable-suspended load. *52nd IEEE conference on decision and control*. 2013 December 10-13; Firenze, Italy. Piscataway: IEEE Press; 2013.p.2269-74.
40. Sreenath K, Michael N, Kumar V. Trajectory generation and control of a quadrotor with a cable-suspended load - A differentially-flat hybrid system. *2013 IEEE international conference on robotics and automation*. 2013 May 6-10; Karlsruhe, Germany. Piscataway: IEEE Press, 2013.p.4888-95.
41. Guo Y, Song SM. Adaptive finite-time backstepping control for attitude tracking of spacecraft based on rotation matrix. *Chin J Aeronaut* 2014;**27**(2):375–82.